

**Analytical modeling for heat transfer in sheared flows of nanofluids**Claudio Ferrari,<sup>1</sup> Badr Kaoui,<sup>2</sup> Victor S. L'vov,<sup>3</sup> Itamar Procaccia,<sup>3</sup> Oleksii Rudenko,<sup>2,4</sup> J. H. M. ten Thije Boonkamp,<sup>4</sup> and Federico Toschi<sup>2,4,5</sup><sup>1</sup>*ISIS R&D Srl, Viale G. Marconi 893, Roma I-00146, Italy*<sup>2</sup>*Department of Applied Physics, Eindhoven University of Technology, Eindhoven, 5600MB, The Netherlands*<sup>3</sup>*Department of Chemical Physics, The Weizmann Institute of Science, Rehovot 76100, Israel*<sup>4</sup>*Department of Mathematics & Computer Science, Eindhoven University of Technology, Eindhoven, 5600MB, The Netherlands*<sup>5</sup>*CNR-IAC, Via dei Taurini 19, 00185 Rome, Italy*

(Received 12 April 2012; published 5 July 2012)

We developed a model for the enhancement of the heat flux by spherical and elongated nanoparticles in sheared laminar flows of nanofluids. Besides the heat flux carried by the nanoparticles, the model accounts for the contribution of their rotation to the heat flux inside and outside the particles. The rotation of the nanoparticles has a twofold effect: it induces a fluid advection around the particle and it strongly influences the statistical distribution of particle orientations. These dynamical effects, which were not included in existing thermal models, are responsible for changing the thermal properties of flowing fluids as compared to quiescent fluids. The proposed model is strongly supported by extensive numerical simulations, demonstrating a potential increase of the heat flux far beyond the Maxwell-Garnett limit for the spherical nanoparticles. The road ahead, which should lead toward robust predictive models of heat flux enhancement, is discussed.

DOI: [10.1103/PhysRevE.86.016302](https://doi.org/10.1103/PhysRevE.86.016302)

PACS number(s): 47.55.pb, 47.57.E-, 47.15.-x, 44.15.+a

**I. INTRODUCTION**

The enhancement of heat transfer by embedded nanoparticles in a fluid subjected to a temperature gradient is an important issue that is expected to help in technological applications such as solar heating, and in various cooling devices, including miniaturized computer processors. Accordingly, many experiments were conducted in the past few decades [1–5]. A breakthrough announcement was made from a group at Argonne National Laboratory, who studied water and oil-based nanofluids containing copper oxide nanoparticles. They found an amazing 60% enhancement in thermal conductivity for only a 5% volume fraction of nanoparticles [6]. However, subsequent research has generated what Ref. [7] referred to as “an astonishing spectrum of results.” Results in the literature sometimes show enhancement in the thermal conductivity compared to the prediction of the Maxwell-Garnett effective-medium theory, and sometimes they show values that are less than that same prediction [1–5]. Confusingly enough, these discrepancies occur even for the same fluid and the same size and composition of the nanoparticles.

Some of these conflicting results were explained by either the formation of percolated clusters of particles (for the case of enhancement with respect to the Maxwell-Garnett prediction) or by surface (Kapitza) resistance (for the case of reduction with respect to the same prediction) [3]. Interestingly enough, enhancement is typically seen in *quiescent* fluids, and one expects that the agglomeration of clusters will become impossible in flows, be they laminar or turbulent. Of course in technological applications, flowing nanofluids may be the rule rather than the exception. Therefore, our aim in this article is to develop models of heat flux in flowing nanofluids where the flow can be either laminar or turbulent. In such systems, we cannot expect an enhancement of heat flux due to the agglomeration of particles (at least at low volume fractions), and for the sake of simplicity we will assume that there is no Kapitza resistance. Since it was reported in the literature that

elongated nanoparticles are superior to spheres in quiescent nanofluids [8], we will study both spheres and spheroids<sup>1</sup> in flowing nanofluids. We will argue that generically elongation may not be advantageous at all, and we will explain why.

For completeness, we will begin by studying quiescent nanofluids under a temperature gradient. We will present extensive numerical simulation that will demonstrate a very good agreement with the Maxwell-Garnett theory for spherical nanoparticles and with the generalization of Nan *et al.* [8] for elongated particles. In the case of flowing nanofluid, we will offer a model that will provide expressions for the heat transfer for different values of the aspect ratio of the particles, for different volume fractions, and for laminar and turbulent flows.

The structure of the paper is as follows. In the next section, we formulate the problem, describe the equations of motion and the numerical procedure, and discuss the dilute suspension approximation. In Sec. III, we describe the results of numerical simulations of spherical and spheroidal particles in a fluid at rest and in a shear flow. In Sec. IV, we develop an analytical model of heat transfer characteristics, i.e., the Nusselt number, and we analyze the model predictions of heat flux enhancement in two limiting cases of very strong Brownian diffusion and weak Brownian diffusion.

**II. NANOFLUIDS IN THE DILUTE LIMIT**

In this section, we formulate the model for dilute nanofluids laden with elongated spheroidal nanoparticles. This includes the basic equation of motion for the velocity and temperature fields and the boundary conditions (with constant velocity and

<sup>1</sup>A spheroid, or an ellipsoid of revolution, is a quadric surface obtained by rotating an ellipse about one of its principal axes; in other words, it is an ellipsoid with two equal semidiameters.

temperature gradients far away from particles). We also present details of the numerical simulations and their validation.

### A. Formulation of the problem and the flow geometry

When nanofluid is very dilute, one can disregard the effect of one particle on another and consider the nanofluid as an ensemble of noninteracting particles [9,10]. One of these is shown in Fig. 1. The center of the spheroidal particle is at the position  $x = y = z = 0$  in the middle of a plane Couette flow between two  $H$ -separated horizontal parallel walls that move in the  $\hat{x}$  direction with opposite velocities  $V_{\pm} = \pm V/2$ . Due to the symmetry, the forces are balanced, and the particle neither migrates nor collides with the walls; the particle's center remains at  $(0,0,0)$ . This allows us to eliminate in the numerics any effect of the particle sweeping parallel to the walls. Note that this effect is absent in homogeneous cases.

We employ periodic boundary conditions along the  $x$  and  $z$  direction. This results in a periodic replication of the computational box (together with the particle) in the  $XZ$  plane, leading to a ‘‘monolayer’’ of an infinite number of periodically distributed particles in the  $XZ$  plane. Remarkably enough (and for reasons that will be explained below), this allows us to reproduce in numerics with a *single particle* the effects of a *finite volume fraction*  $\varphi$  at least up to  $\varphi \lesssim 20\text{--}30\%$ .

The walls are kept at fixed temperatures  $T_{\pm} = T \pm \Delta/2$ . In the absence of particles, these boundary conditions give rise to a vertical temperature gradient  $\nabla_y T = \Delta/H$  and shear  $S = S_{xy} = V/H$  (see Fig. 1).

The spheroidal particle's semiaxes are  $a$  (the longest) and  $b$  (the shortest),  $a \geq b$  (Fig. 1). The thermal diffusivity inside the particle is  $\chi_p$ . The carrier fluid has a kinematic viscosity  $\nu$  and a thermal diffusivity  $\chi_f$ . For simplicity, at this stage we neglect the effect of gravity and the particle mass. The

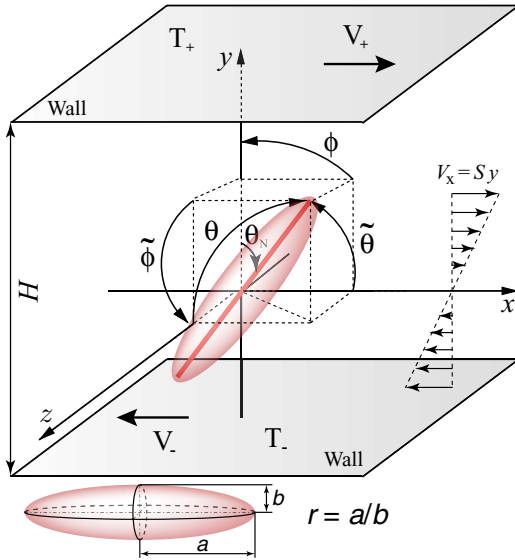


FIG. 1. (Color online) The particle in a plane Couette flow. The largest particle axis is shown as a red rod. The velocity field (far from the particle) is  $(Sy, 0, 0)$ , where the shear  $S = (V_+ - V_-)/H$  in the particle-free flow, with  $H$  being the distance between the walls. For the theoretical development, we assume the creeping flow conditions as in [11–13].

coordinate system and polar angles are given by

$$n_x = \cos \tilde{\theta} = \sin \theta \sin \phi, \quad (1a)$$

$$n_y = \sin \tilde{\theta} \sin \tilde{\phi} = \sin \theta \cos \phi = \cos \theta_N, \quad (1b)$$

$$n_z = \sin \tilde{\theta} \cos \tilde{\phi} = \cos \theta. \quad (1c)$$

We presume that  $\hat{n}$  is a vector for the symmetry axis of the spheroid. Its projections onto the axis are  $n_i$ ,  $i = \{x, y, z\}$ , and  $\theta_N$  is the angle between the particle's largest axis and the  $y$  axis.

In the absence of particles, changing the intensity of the laminar shear flow does not change the heat flux since there is no velocity orthogonal to the wall and the system is homogeneous in the direction parallel to the wall. In the presence of a particle, the shear induces it to rotate, the simplest case being a spherical particle which rotates at a constant angular velocity  $\Omega_z = S/2$  (provided the particle radius is much smaller than the distance to the wall). This rotation induces a vertical flow motion near the particle. The modification of the velocity profile has three consequences. The first directly affects the heat convection in the fluid through a convective contribution  $v_y T$ . The second comes from the particle rotation which brings up the hotter side of the particle during its rotation. The third changes the heat conduction due to a modification of the temperature profiles at the surface of the particle.

In the case of nonspherical particles, the presence of a shear also has a strong influence on the statistical distribution of particle orientations.

### B. Dimensionless parameters

To fix the notation, we list here the most important dimensionless parameters involved in the problem:

$$\text{aspect ratio: } r \equiv a/b, \quad r \geq 1, \quad (2a)$$

$$\text{diffusivities ratio: } k \equiv \chi_p/\chi_f, \quad (2b)$$

$$\text{Prandtl number: } \text{Pr} \equiv \nu/\chi_f, \quad (2c)$$

$$\text{Reynolds number: } \text{Re} \equiv (2a)^2 S/\nu, \quad (2d)$$

$$\text{Peclet number: } \text{Pe} \equiv (2a)^2 S/\chi_p. \quad (2e)$$

Note that the particle's largest axis defines our length scale. Also,

$$\text{Pe} = \text{Re Pr}/k. \quad (3)$$

### C. Basic equations of motion

The dynamical effects previously mentioned can be studied quantitatively by solving the following system of equations for the temperature in the fluid,  $T_f$ , and in the particle,  $T_p$ :

$$\frac{\partial T_f}{\partial t} + (\mathbf{u} \cdot \nabla) T_f = \chi_f \nabla^2 T_f, \quad \frac{\partial T_p}{\partial t} = \chi_p \nabla^2 T_p \quad (4a)$$

together with the boundary conditions,

$$\begin{aligned} \text{at the surface: } & T_f = T_p, \quad \chi_f \nabla T_f = \chi_p \nabla T_p, \\ \text{on the walls: } & T_f(x, 0, z) = T_-, \quad T_f(x, H, z) = T_+. \end{aligned}$$

The fluid velocity in the whole domain can be found by solving the incompressible Navier-Stokes equations:

$$\frac{\partial \mathbf{u}_f}{\partial t} + (\mathbf{u}_f \cdot \nabla) \mathbf{u}_f = -\frac{1}{\rho_f} \nabla p + \nu \nabla^2 \mathbf{u}_f, \quad \nabla \cdot \mathbf{u}_f = \mathbf{0}, \quad (4b)$$

together with nonslip boundary conditions at the surface of the particle and at the walls:

$$\begin{aligned} \mathbf{u}_f(x, 0, z) &= \{V_-, 0, 0\}, & \mathbf{u}_f(x, H, z) &= \{V_+, 0, 0\}, \\ \mathbf{u}_f(x, y, z) &= \mathbf{u}_p(x, y, z) & \text{at the particle's surface.} \end{aligned}$$

Here  $\rho_f$  is the carrier fluid density and  $p$  is the pressure. Clearly, on nanoscales the temperature difference (across a particle) is sufficiently small to allow us to neglect the dependence of the fluid's and particle's material parameters on the temperature, i.e., we take  $\nu$ ,  $\chi_f$ , and  $\chi_p$  as constants.

The dynamics of a neutrally buoyant particle is governed by the equations of the solid body rotation [14]:

$$\begin{aligned} \frac{d \Omega_x^{(b)}}{dt} &= \frac{T_x^{(b)}}{I_x} + \frac{I_y - I_z}{I_x} \Omega_y^{(b)} \Omega_z^{(b)}, \\ \frac{d \Omega_y^{(b)}}{dt} &= \frac{T_y^{(b)}}{I_y} + \frac{I_z - I_x}{I_y} \Omega_z^{(b)} \Omega_x^{(b)}, \\ \frac{d \Omega_z^{(b)}}{dt} &= \frac{T_z^{(b)}}{I_z} + \frac{I_x - I_y}{I_z} \Omega_x^{(b)} \Omega_y^{(b)}, \end{aligned} \quad (4c)$$

where  $\Omega^{(b)}$  is the angular velocity in the body-fixed frame,  $T^{(b)}$  is the torque in the body-fixed frame, and  $I$  is the moment of inertia tensor.

#### D. Numerical approach and its validation

The numerical simulation of the conjugated heat transfer problem given by Eqs. (4) is performed by means of two coupled D3Q19 lattice Boltzmann (LB) equations under the so-called Bhatnagar-Gross-Krook (BGK) approximation [15]. Details of the simulations are presented in Appendix A. Besides purely numerical means, the control of the simulations was done by its comparison with known analytical solutions. As an example, Fig. 2 shows a comparison between the analytical temperature profile (A3) (solid red line) and the numerical profile (black dots) for a moderately big spherical particle [ $H/(2R) = 3.2$ ]. The second test was the comparison in Fig. 10 of the particle's angular velocity theoretically obtained by Jeffery [11] and simulated by our LB realization. For more details, again see Appendix A.

#### E. From single-particle modeling to finite volume fraction

Here we discuss how to relate the contribution of a single particle to the heat flux with the total contribution of many weakly interacting particles randomly distributed in the flow occupying a finite volume fraction  $\phi$ . The first step is to consider the *fully dilute limit*,  $\phi \rightarrow 0$ , in which we can exploit the fact that the particle contribution is additive and proportional to  $\phi$ . In this way, we can introduce the Nusselt number as the ratio between the total heat flux (inside the computational cell) and the conductive heat flux in the basic cell:

$$\text{Nu} = \frac{\langle q \rangle}{\langle q_{\text{cond}} \rangle} = \frac{-\chi_{\text{eff}} \nabla_y T}{-\chi_f \nabla_y T} = \frac{\chi_{\text{eff}}}{\chi_f}, \quad (5)$$

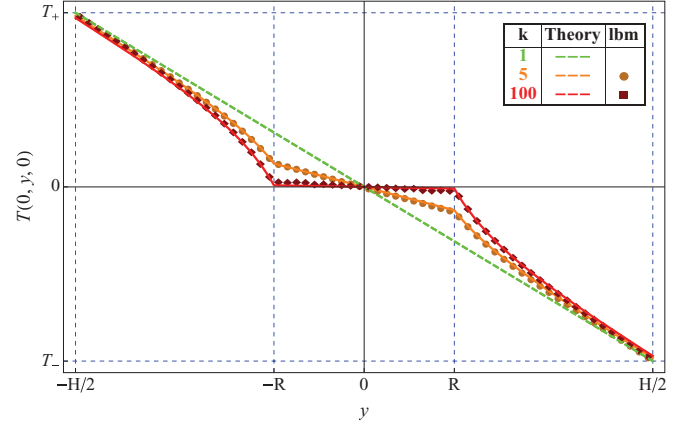


FIG. 2. (Color online) Temperature profile along a line passing through the center of a spherical particle (of radius  $R$ ) in a quiescent fluid. Dashed (green) line, conductive temperature profile in the pure fluid; solid (red) curve, Eq. (A3) [16] for an infinite domain with a temperature gradient; dots, numerical results (at lattice points) with  $k = 5$  (full circles) and  $k = 100$  (squares). The present test was performed with  $\text{Pr} = 1$ ,  $H = 64$ , and  $R = 10$  lattice units.

where  $q$  is the total heat flux,  $q_{\text{cond}} = -\chi_f \nabla_y T$  is the conductive part, and  $\chi_{\text{eff}}$  is the effective heat diffusivity of the composite fluid. Also,  $\nabla_y T \equiv \partial T(x, y, z) / \partial y$ . Without particles,  $\langle q \rangle = \langle q_{\text{cond}} \rangle$  and  $\text{Nu} = 1$ . For *dilute suspensions*, in which  $\phi \ll 1$ ,  $\text{Nu}$  can be expanded in powers of  $\phi$  [17]:

$$\text{Nu} = 1 + \phi K(\phi), \quad (6a)$$

$$K(\phi) = K_1 + K_2 \phi + \dots, \quad (6b)$$

where  $K_i$  are dimensionless constants dependent on the Peclet number, on the particle's aspect ratio,  $r$ , on the relative heat diffusivity,  $k$ , and maybe other parameters such as the Reynolds or Prandtl numbers [see Eqs. (2)], i.e.,  $K_j = K_j(\text{Pe}, r, k, \dots)$ .

As expected, in our simulations the quantity  $(\text{Nu} - 1)$  is indeed proportional to  $\phi$  for  $\phi \lesssim 0.05$ . This allows us to find  $K_1$  as a function of other parameters (2) of the problem.

The next-order term in the expansion (6b), i.e.,  $K_2 \phi$ , contains very important information about how  $\text{Nu}$  depends on  $\phi$  for small but finite values of  $\phi$ . Generally speaking, to get this information from numerics one needs to solve Eqs. (4) for many particles, randomly distributed in space. We demonstrate that this problem can be *simplified tremendously* by reducing it to a *one-particle* case, in which this particle of volume  $V_p = \phi V_{\text{cell}}$  is put in the center of a computational box of volume  $V_{\text{cell}}$  with *periodic boundary conditions* in the horizontal (orthogonal to the temperature gradient)  $x$  and  $z$  directions. In this way, the total system can be considered as constructed from a periodic repetition of the basic elementary cell in the  $x$  and  $z$  directions. Comparing in Sec. III A 1 our numerical results with analytical findings obtained under the assumption of random particle distributions, we see that for *spherical particles* the precise spatial distribution is not essential—what really matters is the actual volume fraction.

The reason for that is quite simple: as one sees in Fig. 2, the deviation from the linear temperature profile becomes

important at distances<sup>2</sup> smaller than the particle diameter  $2R$  for both  $k = 5$  and  $100$ . Thus any nonlinear dependence of  $Nu$  on  $\varphi$  can appear only if the particles are close enough to overlap the deviation from the linear temperature profile. We see from our numerics that this interaction causes a 10% deviation from the straight line in  $Nu$  versus the  $\varphi$  dependence for volume fractions of about 0.1 and more for  $k \leq 100$ . For  $\varphi > 0.1$ , there is some nonlinear dependence of  $Nu$  on  $\varphi$  but it practically coincides for the random and the periodic distributions of spherical particles. Notice that the situation is different for elongated particles: the randomness of the particle orientations is not captured by a periodic simulation. Such simulations describe only very dilute suspension, without nonlinear effects in  $\varphi$ .

### III. TOWARD AN ANALYTICAL MODEL OF THE HEAT FLUX

In this section, we begin by collecting the required information about the dependence of  $K_j$  on the various parameters (2). To do this we consider simple limiting cases, for which some of these parameters are set to zero. We start with the case of spherical particles.

#### A. Spherical nanoparticles

##### 1. Test case: spherical nanoparticles in a fluid at rest

Here we consider the simplest case of a spherical particle ( $r = 1$ ) in a fluid at rest ( $Re = Pe = 0$ ). Chiew and Glandt [18] suggested the following formula for this case:

$$K(k, \varphi) \simeq \frac{3 K_1(k)}{3 - K_1(k)\varphi}, \quad K_1(k) = 3 \frac{k-1}{k+2}, \quad (7a)$$

$$Nu = 1 + \frac{3 K_1(k)\varphi}{3 - K_1(k)\varphi}. \quad (7b)$$

We notice that the expression for  $K_1(k)$  which controls the very dilute limit ( $\varphi \rightarrow 0$ ) is the same as in the Maxwell model [19]. Obviously, for  $k = 1$  one has zero effect, i.e.,  $Nu = 1$ . For  $k \rightarrow \infty$ ,  $K_1 = 3$  and one has maximal possible enhancement (at fixed  $\varphi \ll 1$ ). For  $k = 2$ , one has 25% of this value,  $k = 4$  gives already 50% of the effect,  $k = 10 \Rightarrow 75\%$ ,  $k = 20 \Rightarrow 86\%$ , and  $k = 100 \Rightarrow 97\%$ . Clearly, the larger  $k$  the better, but increasing  $k$  above 100 is not effective.

Actually, Eq. (7) includes also information about the nonlinear dependence  $K(\varphi)$ . However, this dependence is very weak in the relevant range of parameters: e.g., for  $k = 10$  and  $\varphi = 0.2$  the difference between  $K(\varphi)$  and its linear approximation is only 15%. For smaller  $k$ , this difference is even smaller. The physical reason for that was explained at the end of the preceding section.

We tested the prediction of Eq. (7) by simulating the heat flux in a periodic box as explained above in Sec. II and in Appendix A. For the fluid at rest, the (volume-averaged) Nusselt number (as a function of  $\varphi$  at different values of  $k$ ) was measured and is shown in Fig. 3, where the inset shows

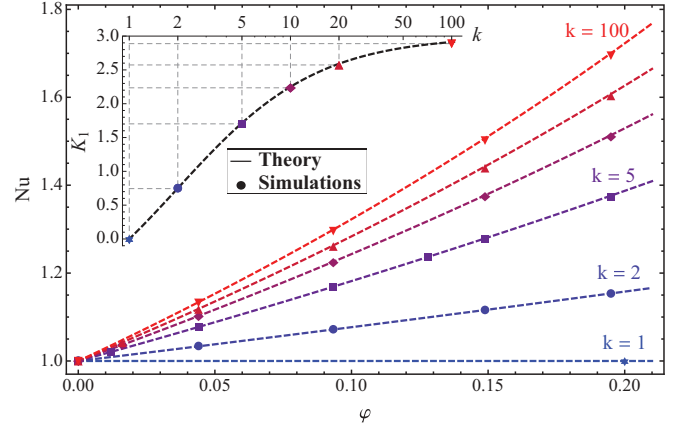


FIG. 3. (Color online) Quiescent fluid, spherical particle in the center.  $Nu(\varphi)$ . Dashed curves, theory, Eq. (7); dots, simulations for different  $k$  (color-coded from “cold” blue,  $k = 1$ , to “hot” red,  $k = 100$ ). Inset:  $K_1(k)$ . Dashed curve, theory, Eq. (7); dots, simulations for different  $k$  (same color code). Notice that for  $128^3$  runs, the accuracy is better than 0.3%, while for  $64^3$  runs it is about 0.7%, and only for very small  $32^3$  runs does it reach the worst value of 1.5%. This means that for our purposes, usually the runs with the  $64^3$  box are fully satisfactory.

$K_1(k)$ . The overall conclusion is that Eq. (7) agrees *extremely* well with all our simulations and thus can be used in modeling the effect of spherical particles in a fluid at rest.

##### 2. Spherical nanoparticles in a shear flow

The next important question is how the particle rotation affects the heat flux. As already mentioned, this rotation induces fluid motions around the particles, thus causing convective contribution to the heat flux. This changes the temperature profile around the particles and, in turn, affects the heat flux inside the particles. To study these issues analytically is extremely difficult and thus numerical simulations can play a crucial role. Due to the fact that we have to deal with a number of parameters, we will carefully examine them starting with the simplest case of spherical particles. Results for spheroidal particles are discussed in Sec. III B2.

We begin by considering the case  $k = 1$ ; such a particle at rest does not affect the heat flux, thus  $Nu = 1$ . In Fig. 4, upper left panel, we present  $Nu(Pe)/Nu(0) - 1$  as a function of  $Pe$  for  $k = 1$  at various volume fractions (from 9.3% to 19.4%), while the inset is showing  $Nu$  versus  $Pe$ . Observing the data, we suggest for  $Pe \lesssim 10$  the following ansatz:

$$Nu(Pe) \simeq Nu(0)[1 + B(k, \varphi)Pe^2], \quad (8a)$$

shown in this panel as a straight dashed (red) line. One sees that Eq. (8a) is approximately valid up to  $Pe \simeq 10$ , where the deviation is about 1%. We note also that for  $k = 1$ , the value of  $B$  is very small,  $B(1, \varphi) \simeq 10^{-4}$ . A similar analysis for  $k = 5$  (cf. Fig. 4, upper right panel) shows that Eq. (8a) fits the data even better with a similar value  $B(5, \varphi) \simeq 2.5 \times 10^{-4}$ .

We see that  $B$  depends weakly on  $\varphi$  but more strongly on  $k$ . Thus, to determine the leading  $k$  dependence, we put a sphere of radius 18 in a  $64^3$  computational volume (all in lattice units); this is equivalent to  $\varphi \simeq 9.3\%$ ; see Fig. 4, lower panels. The  $k$  dependence of  $B(k, \varphi)$  in Eq. (8a) in the range of  $\varphi \simeq 10\%$

<sup>2</sup>It can be shown from Eq. (A3) that the distance should be smaller than  $R|\delta^{-1}(k-1)/(k+2)|^{1/3}$ , where  $\delta$  is the deviation criterion, i.e.,  $|T_f/T_{in} - 1| < \delta$  and  $T_{in} = G_y$ .

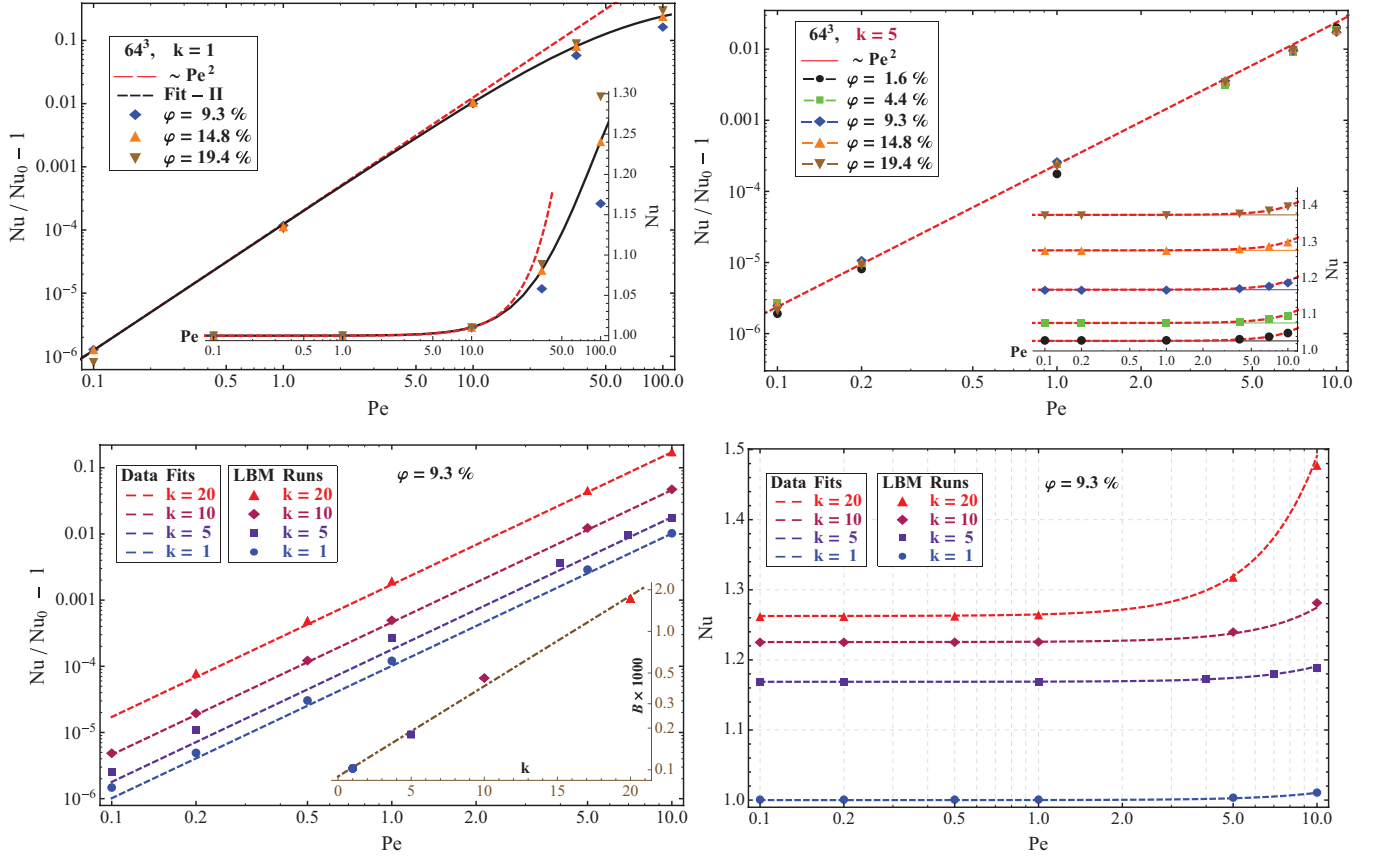


FIG. 4. (Color online) . A spherical particle in a shear (Couette) flow. Upper left panel:  $k = 1$ ,  $\varphi = 9.3\%$ ,  $14.8\%$ , and  $19.4\%$ . Upper right panel:  $k = 5$  for a wider region of  $\varphi$ , but  $Pe$  is limited by 10. Both upper panels show  $Nu(Pe)/Nu_0 - 1$  vs  $Pe$ , and both insets show  $Nu(Pe)$  vs  $Pe$ . Here  $Nu_0 \equiv Nu(0)$ . Dashed (red) line is a fit  $\propto Pe^2$ , cf. Eq. (8a); (color) symbols are simulations with different volume fractions:  $\varphi = 1.6\%$ ,  $4.4\%$ ,  $9.3\%$ ,  $14.8\%$ , and  $19.4\%$ . Solid (black) curve on the upper left panel represents the fit by Eq. (9). Lower panels:  $\varphi = 9.3\%$  and different  $k$  (from “cold” blue,  $k = 1$ , to “hot” red,  $k = 20$ ). Dashed (“temperature”-colored) lines are fits to simulated data (symbols, same colors) by Eq. (8a), left panel, and by combined Eqs. (8) and (7), right panel. Inset on lower left panel:  $B(k, \varphi)$  vs  $k$  at  $\varphi = 9.3\%$ . Dot-dashed (brown) line is the fit to Eq. (8b). Parameters:  $64^3$ ,  $Pr = 1$ , thus  $Re = Pe k$ .

can be fitted by

$$B(k, \varphi) \simeq B_1(\varphi) \exp[B_2(\varphi)k], \quad (8b)$$

$$B_1 \simeq 9 \times 10^{-5}, \quad B_2 \simeq 0.15. \quad (8c)$$

For larger  $Pe \gtrsim 10$ , the  $Nu$  versus  $Pe$  dependence deviates down, as expected, because at  $Pe \rightarrow \infty$  this dependence should saturate. Our analysis shows that this dependence can be fitted with a good accuracy by the formula that generalizes Eq. (8a):

$$\frac{Nu(Pe)}{Nu(0)} - 1 \simeq \frac{B(k, \varphi) Pe^2}{1 + Pe/Pe_1(k) + [Pe/Pe_2(k)]^2}. \quad (9)$$

The upper left panel in Fig. 4 shows by a solid (black) curve how this model works for  $k = 1$  [with  $Pe_1(1) \approx 61$  and  $Pe_2(1) \approx 63$ ].

Having in mind that in many applications related to nanofluids the value of  $Pe$  is smaller than 0.01 and in any case rarely exceeds unity, we reach the conclusion that the convective heat flux around spherical particles and variations of the heat flux inside spherical particles due to their rotation can be neglected. Equation (7) can be used to model the heat flux enhanced by spherical nanoparticles with a finite volume

fraction up to 25% and any actual value of  $k$  in fluids at rest and in shear flows.

The next question to consider is the effect of the particle shape. We will begin with the case of spheroidal particles in fluids at rest.

## B. Spheroidal nanoparticles

### 1. Spheroidal nanoparticles in a fluid at rest

The general expectation is that spheroidal nanoparticles should be able to enhance the heat flux much more effectively than spherical particles. To achieve this, they have to be oriented in the “right” direction, i.e., along with the temperature gradient. Therefore, logically, the study of the heat flux in nanofluids laden with spheroids should begin with the clarification of the effect of the spheroid orientation on the heat flux. In this section, we consider this effect for a given and fixed orientation of the spheroids. For this purpose, we perform numerical simulations of the heat flux with spheroidal nanoparticles in a quiescent fluid ( $Pe = 0$ ) with a temperature gradient, see Fig. 1, taking for concreteness  $k = 5$ .

For different orientations of the spheroid (i.e., different  $\theta_N$ , the angle between the temperature gradient vector and

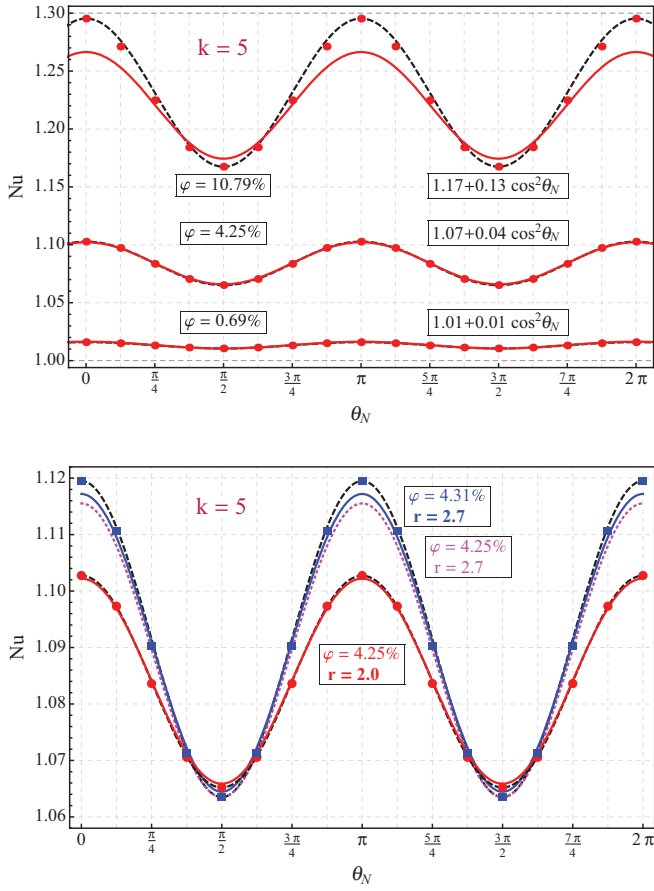


FIG. 5. (Color online) Spheroid in a quiescent fluid at different angles  $\theta_N$ . Both panels:  $k = 5$ ,  $\text{Pr} = 1$ ,  $64^3$ . Symbols, simulations; solid (red or blue) curves, Eq. (11) with appropriate  $r$  and  $\varphi$ ; dashed (black) curves, fits by Eq. (10) to the simulations. Upper panel:  $r = 2$ . Data:  $\varphi \approx 10.79\%$  (upper),  $\varphi \approx 4.25\%$  (middle), and  $\varphi \approx 0.69\%$  (lower). The largest mismatch between the simulations and Eq. (11) is 2.8% at  $\varphi = 10.79\%$ . Lower panel: lower (red) dots:  $\varphi = 4.25\%$ ,  $r = 2.0$ ; and upper (blue) squares:  $\varphi = 4.31\%$ ,  $r = 2.7$ . The dotted (magenta) curve is Eq. (11) with  $\varphi = 4.25\%$  and  $r = 2.7$ . The effect of changing  $r$  is larger than that of  $\varphi$ .

the largest spheroid's axis), we measure different Nusselt numbers: when  $\theta_N = 0$ , spheroids with higher conductivities tend to form a thermal shortcut, thus  $\text{Nu}$  is larger than for  $\theta_N = \pi/2$ , where this shortcut effect is reduced (Fig. 5). Our numerics shows that the dependence of the Nusselt number on the spheroid orientation, i.e.,  $\text{Nu}(\theta_N)$ , for small  $\varphi$  is well described by a simple formula,

$$\text{Nu} = 1 + \varphi \mathcal{K}(k, r, \varphi, \theta_N), \quad (10a)$$

$$\mathcal{K}(k, r, \varphi, \theta_N) = \mathcal{K}_{\min} + \mathcal{K}_{\text{amp}} \cos^2(\theta_N), \quad (10b)$$

and both  $\mathcal{K}_{\min}$  and  $\mathcal{K}_{\text{amp}}$  are functions of  $k$ ,  $r$ , and  $\varphi$ . This equation is a generalization of Eq. (6) for the case of spheroids, and it was suggested in [20] for the limiting case of  $r \rightarrow \infty$  (nanotubes). For large  $\varphi > 5\%$ , deviations become visible. For finite  $\varphi$ , there have been attempts to study the role of the particle shape and form factors, e.g., by Nan *et al.* [8]:

$$\mathcal{K} = \frac{\beta_1 + (\beta_2 - \beta_1) \langle \cos^2 \theta_N \rangle}{1 - \varphi [L_1 \beta_1 + (L_2 \beta_2 - L_1 \beta_1) \langle \cos^2 \theta_N \rangle]}, \quad (11)$$

where  $\beta_j = [L_j + 1/(k-1)]^{-1}$ ,  $j = 1, 2$ ,

$$L_2 = 1 - 2L_1, \\ r > 1 : L_1 = \frac{r}{2(r^2 - 1)} \left[ r - \frac{\text{arccosh}(r)}{\sqrt{r^2 - 1}} \right].$$

Here  $\langle \dots \rangle$  stands for an ensemble average. Clearly, in the case of a single particle as in our simulations, or for a periodic array of particles, the average coincides with the single value. Notice also that for spheres, i.e., when  $r \rightarrow 1$ ,  $L_1 = L_2 = 1/3$  and  $\beta_1 = \beta_2 = K_1$  from Eq. (7), and Eq. (11) simplifies to Eq. (7). For small  $\varphi$ , Eq. (11) coincides with Eq. (10b), giving an analytical expression for  $\mathcal{K}_{\min}$  and  $\mathcal{K}_{\text{amp}}$ .

The range of validity of Eq. (11) was tested by means of a series of simulations at varying angles and volume fractions. The results are reported in Fig. 5. We can conclude that the model in Eqs. (11) well represents the heat flux in the presence of resting spheroidal particles in the relevant range of the parameters  $k$ ,  $r$ , and  $\varphi$ . To apply Eqs. (11) for spheroids in a simple shear flow, we have to find how the ensemble average  $\langle \cos^2 \theta_N \rangle$  depends on  $r$ . For this purpose, we first need to know the orientational distribution function of spheroids in the shear flow. This is the subject of the following subsection.

## 2. Spheroidal nanoparticles in a shear flow

The effect of rotation of elongated spheroidal particles ( $r > 1$ ) is very similar to that of spherical ones ( $r = 1$ ): only the parameters  $B$ ,  $\text{Pe}_1$ , and  $\text{Pe}_2$  of the advanced fit (9) depend on the aspect ratio  $r$ . As an example, we presented in Fig. 6 a preliminary result of the computed and fitted  $\text{Nu}(\text{Pe})$  dependence for  $r = 5$  and  $k = 5$ . In this case,  $B \approx 5.3 \times 10^{-5}$ ,  $\text{Pe}_1 \approx 5.2$ , and  $\text{Pe}_2 \approx 30.3$ . This is interesting to compare with the respective parameters for  $r = 1$  and  $k = 5$ :  $B \approx 2.5 \times 10^{-4}$ ,  $\text{Pe}_1 \approx 61$ , and  $\text{Pe}_2 \approx 63$ . One sees that the  $\text{Pe}$  enhancement of the heat flux with elongated particles is smaller than for spherical ones [ $B(r > 1) < B(r = 1)$ ] and it saturates at smaller  $\text{Pe}$ :  $\text{Pe}_1(r > 1) < \text{Pe}_1(r = 1)$  and  $\text{Pe}_2(r > 1) < \text{Pe}_2(r = 1)$ . Moreover, the overall conclusion that  $\text{Nu}(\text{Pe})$  is almost  $\text{Pe}$ -independent for  $\text{Pe} \lesssim 1$  remains valid,

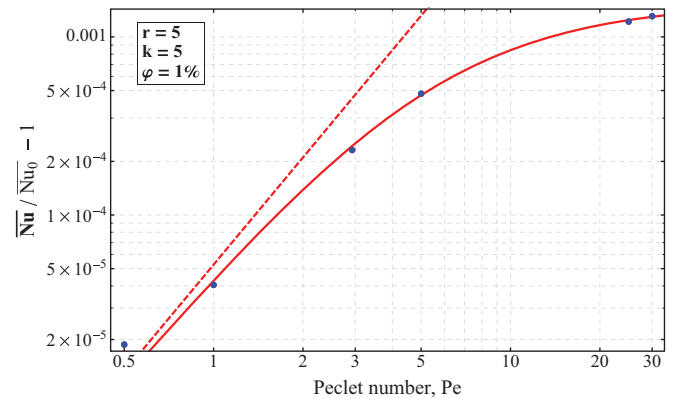


FIG. 6. (Color online) Example of advanced fit (9) for a spheroid  $r = 5$ ,  $k = 5$ . (Blue) dots, numerical data; solid (red) curve, fit by Eq. (9) with  $B \approx 5.3 \times 10^{-5}$ ,  $\text{Pe}_1 \approx 5.2$ , and  $\text{Pe}_2 \approx 30.3$ . Dashed (red) line is  $B \text{Pe}^2$ . Here  $\bar{\text{Nu}}$  is the time-averaged  $\text{Nu}(t)$  over the period of rotation (determined in the simulations), and  $\bar{\text{Nu}}_0$  is the time-averaged  $\text{Nu}(t)$  for the smallest available  $\text{Pe}$ , e.g.,  $\text{Pe} = 0.01$ .

thus the model developed above in Eq. (11) with Eq. (24) may be safely used for nanoparticle-laden flows at  $Pe \lesssim 1$ .

#### IV. ANALYTICAL MODEL OF HEAT TRANSFER IN A LAMINAR SHEAR FLOW

In this section, we develop an analytical model for  $Nu(k, r, \varphi)$ .

##### A. Orientational statistics of elongated nanoparticles

###### 1. Fokker-Planck equations for the orientational PDF

In order to study the orientational statistics of elongated nanoparticles, we consider the probability distribution function (PDF),  $\mathcal{P}(\theta, \phi, t)$ , which is the probability  $P(\theta, \phi, t)$  of finding any particular spheroid with its axis of revolution in the interval  $[\theta, \theta + d\theta] \times [\phi, \phi + d\phi]$  on the unit sphere. The PDF is then defined by

$$P(\theta, \phi, t) = \mathcal{P}(\theta, \phi, t) \sin \theta d\theta d\phi. \quad (12)$$

It was shown by Burgers [21] that  $\mathcal{P}(\theta, \phi, t)$  satisfies a generalized Fokker-Planck equation in the presence of a shear:

$$\frac{\partial \mathcal{P}}{\partial t} = -\nabla \cdot (\mathbf{w}\mathcal{P}) + D_r \nabla^2 \mathcal{P}, \quad (13)$$

where  $\mathbf{w} \equiv (0, \dot{\theta}, \dot{\phi} \sin \theta)$  is the relative velocity on the unit sphere of the axis of revolution for a particle with instantaneous orientation  $(\theta, \phi)$  ignoring all Brownian effects. The explicit form of this equation in spherical coordinates is

$$\frac{\partial \mathcal{P}(\theta, \phi)}{\partial t} + \frac{1}{\sin \theta} \left[ \frac{\partial}{\partial \theta} F_\theta \sin \theta + \frac{\partial}{\partial \phi} F_\phi \right] = 0. \quad (14a)$$

Here  $F_\theta$  and  $F_\phi$  are the  $\theta$  and  $\phi$  projections of the probability density fluxes that have two shear-induced contributions, one proportional to  $w$  and the other to the rotational diffusion coefficient,  $D_r$ :

$$F_\theta = \left[ \frac{\partial \theta}{\partial t} - D_r \frac{\partial}{\partial \theta} \right] \mathcal{P}(\theta, \phi), \quad (14b)$$

$$F_\phi = \left[ \sin \theta \frac{\partial \phi}{\partial t} - \frac{D_r}{\sin \theta} \frac{\partial}{\partial \phi} \right] \mathcal{P}(\theta, \phi). \quad (14c)$$

Burgers in Ref. [21] derived the rotational diffusion coefficient,  $D_r$ , of elongated rigid spheroids of revolution:

$$D_r = \frac{k_B T}{4\mu V} \left[ \frac{r^2 + 1}{r^2 K_3 + K_1} \right]^{-1}. \quad (15a)$$

Here  $\mu$  is the dynamical fluid viscosity,  $k_B = 1.374 \times 10^{-16}$  erg/deg K is the Boltzmann constant, particle volume

$$V = \frac{4}{3}\pi a^2 b, \quad 2a = d, \quad b = ra, \quad r \geq 1, \quad \text{and}$$

$$K_3 = \int_0^\infty \frac{rdx}{(r^2 + x)^{3/2}(1+x)} \quad (15b)$$

$$= \frac{2}{r^2 - 1} \left[ 1 - \frac{r \operatorname{arccosh}(r)}{\sqrt{r^2 - 1}} \right] \rightarrow 2 \frac{\ln(2r/e)}{r^2},$$

$$K_1 = \int_0^\infty \frac{rdx}{(r^2 + x)^{1/2}(1+x)^2}$$

$$= \frac{r}{r^2 - 1} \left[ r - \frac{\operatorname{arccosh}(r)}{\sqrt{r^2 - 1}} \right] \rightarrow 1. \quad (15c)$$

This asymptotics is formally valid for  $r \gg 1$ , but gives better than 10% accuracy already for  $r > 4$ , allowing us to suggest the approximate ‘‘practical’’ formula

$$D_r \simeq \tilde{D}_r = \frac{k_B T}{4\mu V} \frac{\ln(4r^2/e)}{(r^2 + 2r/3 - 1)}, \quad (16)$$

which works with an accuracy of about 10% for any  $r \geq 1$  and with better than 5% accuracy for  $r > 10$ .

The complete analysis of Eqs. (14) is very involved; see, e.g., Refs. [12] and [13]. We consider only the small-diffusion limit; see the next subsection.

###### 2. Statistics of elongated nanoparticles in the small-diffusion limit

Jeffery [11] has shown that if inertial and Brownian motion affects are completely neglected, then the motion of the axis of revolution of a spheroidal particle is described by

$$\tan \phi = r \tan \tau, \quad (17a)$$

$$\begin{aligned} \tan \theta &= C \sqrt{\cos^2 \tau + r^2 \sin^2 \tau} \\ &= Cr(r^2 \cos^2 \phi + \sin^2 \phi)^{-1/2}, \end{aligned} \quad (17b)$$

where  $\tau = t/T_r$  with  $T_r = (r + 1/r)/S$ , and the constant of integration  $C$  is called the (Jeffery) orbit constant.

To analyze the small-diffusion limit, we introduce two time scales. The first one defines the periodic motion that a nanoparticle with a finite  $r$  exhibits:  $T_r = T_J/2\pi$ , where  $T_J = 2\pi(r + 1/r)/S$  is the Jeffery’s period. The second time scale is determined by the inverse shear,  $T_S = S^{-1}$ . Clearly, for large  $r$  this is a much shorter time scale, so for  $r \gg 1$ ,

$$T_r \approx r/S = r T_S. \quad (18)$$

It means that the particles spend most of their time near pre- and postaligned states. If the Brownian diffusion is small enough such that  $T_{\text{dif}} = D_r^{-1} \gg T_r$ , one can neglect the effect of the Brownian motion on the dynamic motions of particles along Jeffery orbits [11] even during their slow time evolution. In this case, the stationary Fokker-Planck equation (13) takes the simple form

$$\nabla \cdot (\mathbf{w}\mathcal{P}) = 0. \quad (19)$$

This equation can be solved [12,13] giving

$$\mathcal{P}(\theta, \phi) = f(C, r) \mathcal{P}_C(\theta, \phi), \quad (20a)$$

$$\mathcal{P}_C(\theta, \phi) = (r \sin \theta \cos^2 \theta \sqrt{\cos^2 \phi + \sin^2 \phi / r^2})^{-1}, \quad (20b)$$

where  $\mathcal{P}_C(\theta, \phi)$  is the PDF along a particular Jeffery orbit with a given integration constant  $C$ , and  $f(C, r)$  is the probability

to occupy this orbit. This function is normalized as follows:

$$\int_0^\infty f(C)dC = \frac{1}{4\pi}.$$

$f(C,r)$  was found in [12] for the following limiting cases:

$$f(C,r=1) = \frac{1}{4\pi} \frac{C}{(C^2+1)^{3/2}}, \quad (21a)$$

$$f(C,r \gg 1) \simeq \frac{1}{\pi} \frac{C}{(4C^2+1)^{3/2}}, \quad (21b)$$

$$f(C,r \ll 1) \simeq \frac{1}{\pi} \frac{Cr^2}{(4r^2C^2+1)^{3/2}}. \quad (21c)$$

Note that Eq. (21a) is exact, providing a consistency check of the present approach by comparison with spherical particles. The asymptotic, Eq. (21b), is very accurate for  $r > 20$ , but already for  $r \gtrsim 4$  it provides reasonable accuracy (better than  $\sim 10\%$ ).

The analysis of Eqs. (21) together with the available numerical solutions for  $r = 0.26$  and  $3.86$  [12] allowed us to suggest the following approximation:

$$f(C,r) \simeq \frac{C/(r+1/r)^2}{\pi [1+4C^2/(r+1/r)^2]^{3/2}}. \quad (22)$$

A comparison of this approximation with the exact numerical solution provided in Ref. [12] is presented in Fig. 7, upper panel. One sees that Eq. (22) fits the numerical data with an accuracy better than 5%. This is more than enough for our purpose to offer an approximate formula for  $\langle \cos^2 \theta_N \rangle$  as a function of  $r$ ; see below.

Next we use the fact that Jeffery orbits do not intersect on the unit sphere. In other words, fixing  $C$  results in a relation between  $\theta$  and  $\phi$  along an orbit. This relationship is obtained by inverting Eq. (17b):

$$C = C(\theta, \phi) = \tan \theta \sqrt{r^{-2} \sin^2 \phi + \cos^2 \phi}. \quad (23)$$

Substituting this function into any one of Eqs. (21), we get  $f(C,r)$  for a given regime of  $r$ . This is then substituted in Eqs. (20), leading finally to a solution of the orientational PDF  $\mathcal{P}(\theta, \phi)$ , which can be used for averaging Eqs. (11) in the case of weak Brownian motion. As a consistency check of the approach, one can consider the trivial case  $r = 1$ . From Eq. (23) one finds  $C = \tan \theta$ , then from Eq. (21a)  $f(C) = \sin \theta \cos^2 \theta / 4\pi$ , and finally from Eq. (20b)  $\mathcal{P}_C = 1 / \sin \theta \cos^2 \theta$ . As a result, one has for the sphere  $\mathcal{P} = 1/4\pi$ , as expected.

For moderate and strong Brownian rotational motion, the notion of separate Jeffery orbits becomes irrelevant. In this case, we need to solve Eq. (13) without approximations. Once this equation is solved, we can compute  $\langle \cos^2 \theta \rangle$  and substitute the answer in Eqs. (11). To achieve this in the most general case is not a simple task, and here we satisfy ourselves with the two limiting cases of very large and very small rotational diffusion. The second case was discussed above. For the case of very strong rotational diffusion, we can use the same Eqs. (11), but averaged with a uniform PDF  $\mathcal{P}(\theta, \phi) = 1/4\pi$ . This is because the very strong rotational diffusion tends to distribute particle motions around the Jeffery orbits uniformly. The corrections

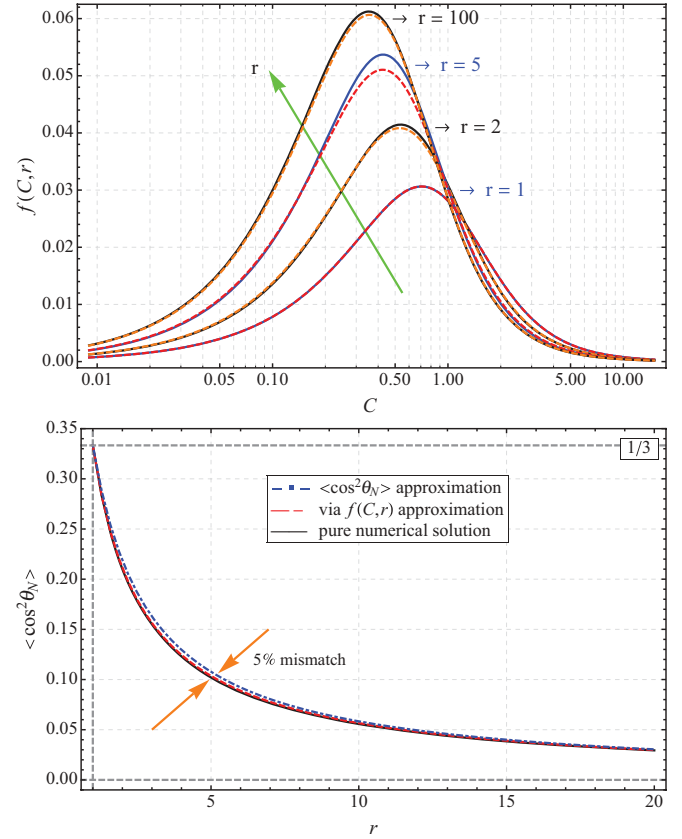


FIG. 7. (Color online) . Upper panel: Comparison of “exact numerical” solutions obtained from Eq. (19) (solid lines) and approximate solutions obtained from Eq. (22) for different  $r$  (dashed lines). There is a visible difference (about 5% in the value of maximum) only for  $r = 5$ . Lower panel: Comparison of the dependence of  $\langle \cos^2 \theta \rangle$  vs  $r$  obtained by (a) applying “exact numerical” PDF (black solid line), (b) approximate analytical PDF, Eq. (22) (red dashed line), and (c) analytical approximation for this dependence, Eq. (24) (blue dot-dashed line).

up to  $O(S/D_r)^2$  to such a uniform distribution may be found in Refs. [22,23].

## B. Predictions of the model

### 1. Spheroidal nanoparticles in a strong Brownian diffusion limit

With very strong Brownian diffusion, the particles are oriented completely randomly, and  $\langle \cos^2 \theta_N \rangle = 1/3$ . In this case, Eqs. (10) and (11) give the results reported in Fig. 8, upper panels. The upper left panel shows  $Nu$  versus  $r$  dependence for various  $k$  from 1 to 8600 and  $\infty$  with volume fraction  $\varphi = 1\%$ . These results are rather obvious: for  $k = 1$ , one obtains  $Nu = 1$ , i.e., no enhancement; the larger the  $k$ , the larger the heat flux enhancement; for any finite  $k$ , there is a saturation of  $Nu(r)$  for  $r \rightarrow \infty$ . The value of  $(Nu - 1)$  may be huge for spheroids (essentially, rodlike particles at  $r \gg 1$ ), e.g., for  $k = 8600$  (diamond in water),  $Nu - 1 \simeq 30$ , while for spherical particles ( $r = 1$ ),  $Nu - 1 = 0.03$  at the same volume fraction  $\varphi = 0.01$ . The values of  $Nu(k,r)$  are bounded, i.e.,  $Nu(1,r) \leq Nu(k,r) \leq Nu(\infty,r)$ .

The upper right panel shows  $Nu$  versus  $k$  dependence at  $\varphi = 1\%$  for three values of  $r$ : 1, 5, and 10. The values of  $Nu(k,r)$  are

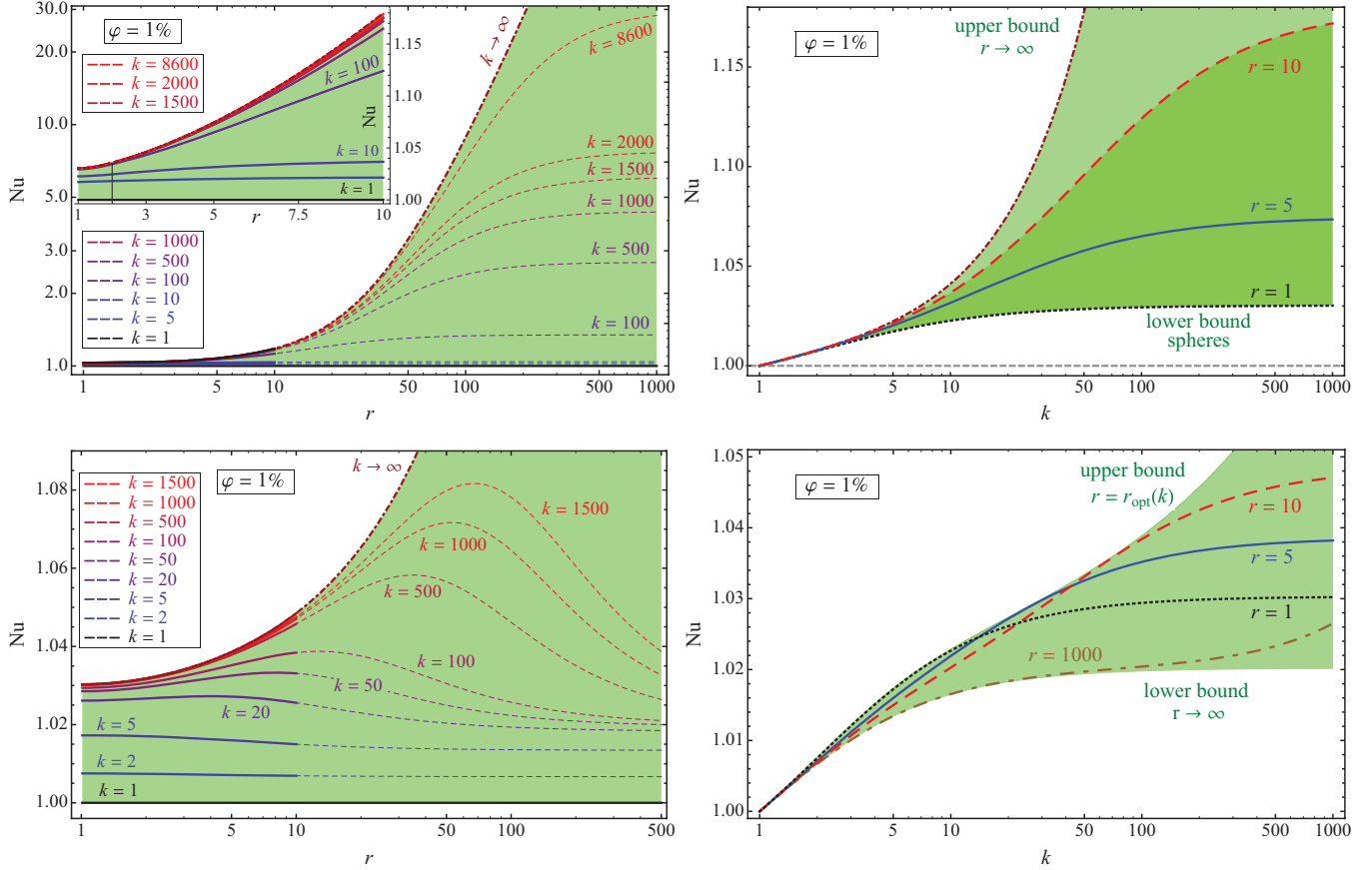


FIG. 8. (Color online)  $\varphi = 1\%$ ,  $r_0 = 10$ . Upper panels: *strong* Brownian diffusion limit:  $\langle \cos^2 \theta_N \rangle \rightarrow 1/3$ ; lower panels: *weak* Brownian diffusion limit. Left panels: Nusselt number  $Nu$  vs particle aspect ratio  $r$  for various heat diffusivity ratios,  $k$ : solid curves for  $r < r_0$ , dashed curves for  $r > r_0$  (the region where the particles may, in principle, start touching each other). The shaded (green) area is the region of all possible  $Nu(k, r)$  at  $\varphi = 0.01$ : the lower bound is given by  $Nu(1, r)$ , the upper one is  $Nu(\infty, r)$ . Right panels:  $Nu$  vs  $k$  for various,  $r$ . Dotted (black) curve is for  $r = 1$ , spherical particles; solid (blue) curve is for  $r = 5$ ; dashed (red) curve is for  $r = 10$ ; and dot-dashed (brown) curve is for  $r = 1000$ , lower panel, or  $r \rightarrow \infty$ , upper panel. The shaded (green) area is the region of all possible  $Nu(k, r)$  at  $\varphi = 0.01$ : the lower bound is  $Nu[k, 1]$  in the upper panel and  $Nu(k, \infty)$  in the lower panel, while the upper bound is  $Nu(k, \infty)$  in the upper panel and  $Nu[k, r_{\text{opt}}(k)]$  in the lower panel, where  $r_{\text{opt}}(k)$  maximizes  $Nu$  at every  $k$ ; see the text for additional details. The geometrical constrain imposes  $1 \leq r \leq \max(r_{\text{opt}}, 10)$  for  $\varphi = 1\%$ .

bounded, too:  $Nu(k, 1) \leq Nu(k, r) \leq Nu(r, \infty)$ . Here, the more elongated the particle is (larger  $r$ ), the better the enhancement.

And last but not least, elongated particles may touch each other much more easily. As we show in Appendix B, the basic geometrical requirement that the mean interparticle distance is less than the largest particle size means that  $r < r_0 \equiv \varphi^{-1/2}$ , which is the basic criterion of the dilute limit. The  $Nu(r)$  dependence for  $r < r_0$  is shown by solid curves, while the region  $r > r_0$  is shown by dashed curves in Fig. 8, left panels. Provided  $r \leq 10$  at  $\varphi = 1\%$ , the enhancement may still be considered large but not huge: for  $k = 5$ , the saturation level of  $(Nu - 1)$  is about 0.25, while for spheres  $Nu - 1 \approx 0.017$ .

The conclusion in the case of very strong Brownian diffusion is that the particles with larger  $k$  and  $r$  bring larger heat flux enhancement in the laminar shear flow.

## 2. Spheroidal nanoparticles in a weak Brownian diffusion limit

To complete the calculations of the  $Nu(r)$  dependence in a weak Brownian diffusion limit in the framework of model (11), we have to find  $\langle \cos^2 \theta_N \rangle$  versus  $r$ . To make a long story

short, we compared in Fig. 7, lower panel, the dependence of  $\langle \cos^2 \theta_N \rangle$  versus  $r$  obtained by numerically solved the PDF, Eq. (19) (see Refs. [12,13] for more details), shown by a (black) solid curve, and by the approximate analytical PDF, Eq. (22), shown by a (red) dashed curve. As one can see, these two dependences coincide within the linewidth. Moreover, by a careful analysis of various limiting cases, we suggested the following simple model dependence:

$$\langle \cos^2 \theta_N \rangle \simeq \frac{2}{6 + \pi(r - 1)}, \quad (24)$$

shown in Fig. 7, lower panel, as a (blue) dash-dotted curve. Equation (24) fits the exact dependence with an accuracy of 5%. Therefore, Eqs. (11) and (24) can be used in our analysis to make predictions on the thermal properties in the limit of small Brownian diffusion of fluids laden with spheroidal nanoparticles of different aspect ratios and different thermal conductivity ratios with a Peclet number up to unity. Corresponding results are shown in Fig. 8, lower panels.

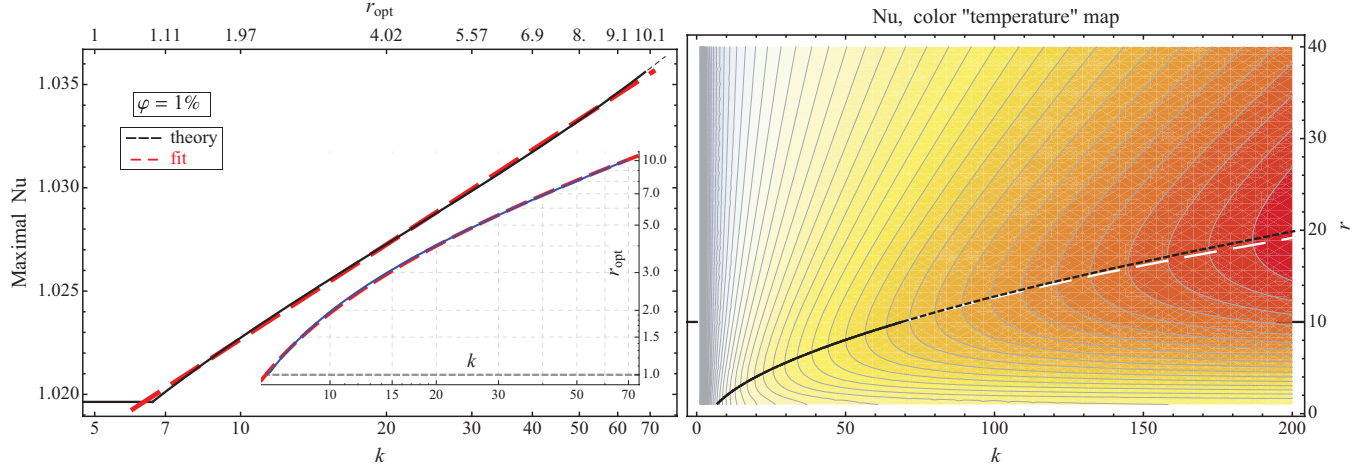


FIG. 9. (Color online) . *Weak Brownian diffusion limit*,  $\varphi = 1\%$ ,  $r_0 = 10$ . Left: The largest reachable Nusselt number,  $\text{Nu}(k, r_{\text{opt}})$ , solid (black) curve ( $r_{\text{opt}}$  maximizes  $\text{Nu}$  for a given  $k$ ). Dashed (red) line is the fit by  $\text{Nu}_{\text{max}}^{\text{fit}} \approx 1 + \varphi[0.75 + 0.66 \ln(k)]$ . Inset:  $r_{\text{opt}}$  vs  $k$ , solid (blue) curve, and the fit  $r_{\text{opt}}^{\text{fit}} \approx -3.03 + 1.57\sqrt{k}$  for  $1 \leq r_{\text{opt}} \leq 10$ , dashed (red) line. Since  $\varphi = 0.01 \ll 1$ , this fit may be considered as  $\varphi$ -independent for  $\varphi \leq 1\%$ . Right: Contour-density plot of  $\text{Nu}(k, r)$  color-coded with the “temperature” map: the larger the value of  $\text{Nu}$ , the warmer the color; contours show isovalues of  $\text{Nu}$ . Thick (black) solid and dashed curves represent those pairs of  $(k, r)$  for which  $\text{Nu}$  is maximal [i.e., solid (blue) curve in the inset]; the solid curve is for  $r < r_0$ , and the dashed one is for  $r > r_0$ . Wide-dashed (white) curve is the  $r_{\text{opt}}^{\text{fit}}(k)$  fit.

The lower left panel in Fig. 8 shows  $\text{Nu}(r)$  for different  $k$  and  $\varphi = 0.01$ , at which the Maxwell-Garnett limit of  $\text{Nu} - 1$  for spherical particles ( $r = 1$ ) is  $3\varphi = 0.03$ . Notice that the  $\text{Nu}(r)$  dependence is not monotonic and has a maximum at some  $r = r_{\text{opt}}$ , which depends on  $k$ . The reason for this is the competition of two effects: more elongated nanoparticles make a larger contribution to the heat flux when their longer axis is aligned with the temperature gradient, which is orthogonal to the velocity gradient (shear) in our case. However, longer nanoparticles are affected more readily by the shear, which tends to orient them in the unfavorable direction orthogonal to the temperature gradient; then their contribution to the heat flux is even less than that of the spherical particles (cf. Fig. 5). Again, the values of  $\text{Nu}(k, r)$  are bounded, i.e.,  $\text{Nu}(1, r) \leq \text{Nu}(k, r) \leq \text{Nu}(\infty, r)$ .

The lower right panel in Fig. 8 shows  $\text{Nu}(k)$  for different aspect ratios,  $r$  at  $\varphi = 1\%$ . This is again a consequence of the above-described competition. The values of  $\text{Nu}$  are bounded by  $\text{Nu}(k, \infty) \leq \text{Nu}(k, r) \leq \text{Nu}[k, r_{\text{opt}}(k)]$ . Moreover, for  $1 \leq k \lesssim 7$  the optimal nanoparticle shape is spherical.

As seen in Fig. 8, lower left panel, there exists a maximum of  $\text{Nu}(r = r_{\text{opt}})$  for a given  $k$ . This maximal Nusselt number at its maximizing (optimal)  $r = r_{\text{opt}}(k)$  is shown in Fig. 9, left, as a function of  $k$  for  $\varphi = 0.01$ . For  $k > 7$ , the maximal  $\text{Nu}$  behaves like

$$\text{Nu}_{\text{max}}^{\text{fit}} \approx 1 + \varphi [0.75 + 0.66 \ln(k)], \quad \varphi = 0.01. \quad (25a)$$

Since here  $\varphi \ll 1$ , the part in parentheses may be considered as  $\varphi$ -independent, thus the fit (25a) may be used at any  $\varphi \leq 1\%$ .

The right panel of Fig. 9 exhibits a contour-density plot of  $\text{Nu}(r, k)$  at  $\varphi = 0.01$ . Thick (black) solid and dashed curves show the  $r_{\text{opt}}(k)$  dependence (the solid curve is for  $r < r_0$  and the dashed one is for  $r > r_0 = \varphi^{-1/2} = 10$ ). The inverse dependence  $k(r_{\text{opt}})$  is easy to obtain with a symbolic computation software by solving  $\partial \text{Nu}(r, k, \varphi) / \partial r = \partial \mathcal{K}(r, k, \varphi) / \partial r = 0$  at  $r = r_{\text{opt}}$ , although the answer is too cumbersome to be shown

here. However, our analysis reveals that  $r_{\text{opt}} \sim \sqrt{k}$ , and for  $\varphi = 0.01$  and  $1 \leq r_{\text{opt}} \leq 10$ ,

$$r_{\text{opt}}^{\text{fit}}(k) \approx -3.03 + 1.57\sqrt{k}, \quad \varphi = 0.01. \quad (25b)$$

This dependence is shown in Fig. 9, right, as a wide-dashed (white) curve, which deviates from the analytical solution  $r_{\text{opt}}(k)$  for  $r_{\text{opt}} > 10$ . Again, since  $\varphi \ll 1$ , the fit (25b) may be used<sup>3</sup> at any  $\varphi \leq 1\%$ .

In conclusion, we should notice that the rich information about heat flux enhancement, shown in the four panels of Fig. 8, is just an illustration of the analytical dependence  $\text{Nu}(\varphi, k, r)$  given by the analytical expressions (11) and (24). This is an important result of our modeling.

## V. CONCLUSIONS

We presented a study of the physics of the heat flux in a fluid laden with nanoparticles of different physical properties (shape, thermal conductivity, etc). We developed an analytical model for the effective thermal properties of dilute nanofluid suspensions. Our model accounts for nanoparticle rotation dynamics including the fluid motion around the nanoparticles. We note that our model reproduces the classical Maxwell-Garnett model in the appropriate static limits.

We used a combination of theoretical models and numerical experiments in order to make progress from the simplest case of spherical nanoparticles in a quiescent fluid to the most general case of rotating spheroidal particles in shear flows. The physical ingredient that we consider is the exact dynamics of particles in shear flows. This sets our model apart from most of the models introduced so far, which have focused only on

<sup>3</sup>According to Eqs. (10a) and (11) for  $\varphi \ll 1$ ,  $\partial \text{Nu} / \partial r \approx \partial [\beta_1 + (\beta_2 - \beta_1) \langle \cos^2 \theta_N \rangle] / \partial r$ , which is a function of  $(k, r)$  only.

the static properties of the nanoparticle suspension to explain the thermal properties of thermal colloids. Our model starts from the realization that particles (spherical or spheroidal) in the presence of a gradient of the velocity field are induced to rotate. The dynamics of rotation is absolutely nontrivial, but it has been studied at length as it corresponds (for the case of a laminar and stationary shear flow) to the Jeffery orbits.

The particle rotation dynamics has a double influence on the thermal properties of the nanofluid. First, particle rotation induces fluid motions in the proximity of the particles. This in turn can enhance the thermal fluxes by means of advective motion along the direction of the temperature gradient. Second, the Jeffery dynamics of particles leads to a statistical distribution of particle orientation that depends on a multitude of parameters, e.g., the particle aspect ratio, the shear intensity, as well as the intensity of thermal fluctuations. The statistical distribution of particle orientation has a dramatic influence on the heat flux: an elongated particle oriented along the temperature gradient increases the thermal flux, while a particle with perpendicular orientation reduces it.

The statistical orientation of particles can thus produce a mixed effect with a nontrivial dependence on the particle aspect ratio. More elongated particles can enhance the heat flux because of the stronger contribution when properly aligned to the temperature gradient. However, because of shear, more elongated particles are also spending more time in the unfavorable direction (i.e., perpendicular to the temperature flux), thus reducing the thermal conductivity of the fluid.

By means of numerical approximations, we are able to provide closed expressions for the effective conductivity of the fluid under several flow regimes and for several physical parameters. Our model extends classical models considerably for nanofluid heat transfer, such as, e.g., the Maxwell-Garnett model, and it may help to rationalize some of the recent experimental findings. In particular, we suggest that experiments should consider more carefully measurements performed in quiescent and under flowing conditions: the particle dynamics may lead to very different thermal properties in the two cases.

Finally, the next steps toward a robust predictive model for the heat transfer in nanofluids should include the effects of surface (Kapitza) resistance and nanoparticle aggregation. Furthermore, it would also be extremely important to extend the model to the case of heat flux in turbulent nanofluids, as this case is very relevant to many applications. In the presence of turbulence, particular attention should also be paid to the effect on the drag caused by the presence of spherical, rodlike, or possibly even deformable nanoparticle inclusions.

## ACKNOWLEDGMENTS

We acknowledge financial support from the EU FP7 project “Enhanced nano-fluid heat exchange” (HENIX), Contract No. 228882.

## APPENDIX A: NUMERICAL APPROACH

The numerical simulation of the conjugated heat transfer problem, Eqs. (4a)–(4c), is performed by means of two coupled D3Q19 lattice Boltzmann (LB) equations under the BGK approximation [15] (for velocity and temperature fields) and

molecular-dynamics simulations (for particles motion):

$$f_l(\mathbf{x} + \mathbf{c}_l, t + 1) - f_l(\mathbf{x}, t) = \frac{f_l^{\text{eq}}(\mathbf{x}, t) - f_l(\mathbf{x}, t)}{\tau_f}, \quad (\text{A1a})$$

$$g_l(\mathbf{x} + \mathbf{c}_l, t + 1) - g_l(\mathbf{x}, t) = \frac{g_l^{\text{eq}}(\mathbf{x}, t) - g_l(\mathbf{x}, t)}{\tau_g}, \quad (\text{A1b})$$

where  $f_l(\mathbf{x}, t)$  is the lattice Boltzmann distribution function for particles at  $(\mathbf{x}, t)$  with velocity  $\mathbf{c}_l$  (with  $l = 0, \dots, 18$  for D3Q19), and  $f_l^{\text{eq}}$  is its equilibrium distribution;  $g_l(\mathbf{x}, t)$  is the distribution function associated with the temperature and  $g_l^{\text{eq}}$  is its equilibrium distribution. The first LB equation, Eq. (A1a), evolves the fluid flow outside of the rigid particle, and its momentum is coupled with the particle boundaries by means of a standard scheme, as proposed by Ladd [24]. The second LB equation, Eq. (A1b), evolves the temperature field, treated as a passive scalar as proposed in [25], solving the conjugated heat transfer problem simply by means of adjusting the thermal conductivity to the correct values in the fluid and inside the particle [Eqs. (4a) and (4b)]. Thermal and velocity boundary conditions, at the top and bottom walls, impose the LB populations to equal the equilibrium populations (corresponding to the desired velocity and temperature). This approach can produce small temperature and velocity slip which are kept into account by measuring the effective temperature and velocity profiles, thus increasing the accuracy. The code employed is fully parallelized by means of MPI libraries [26], thus allowing large system sizes, which are important to study the influence of finite-size effects.

Density, momentum, and temperature are defined locally at  $(\mathbf{x}, t)$  as coarse-grained (in velocity space) fields of the distribution functions,

$$\rho_f = \sum_l f_l, \quad \rho_f \mathbf{u}_f = \sum_l \mathbf{c}_l f_l, \quad \rho_f T_f = \sum_l g_l. \quad (\text{A2})$$

A Chapman-Enskog expansion [27] around the local equilibria  $f_l^{\text{eq}}(\mathbf{u}, \rho)$  and  $g_l^{\text{eq}}(\mathbf{u}, T)$  [28] leads to the equations for temperature and momentum, (4a) and (4b): the streaming step on the left hand side of (A1a) reproduces the inertial terms in the hydrodynamical equations, whereas the diffusive terms (dissipation and thermal diffusion) are closely connected to the relaxation (toward equilibrium) properties on the right hand side, with  $\nu$  and  $\chi$  related to the relaxation times  $\tau_f, \tau_g$  [15].

## 1. Conjugated heat transfer for a spherical particle at rest

Consider a spherical particle of radius  $R$  immersed in a quiescent fluid, in which a constant temperature gradient,  $\mathbf{G}$ , is maintained. The temperature distribution is [16]

$$T_p(\mathbf{r}) = \frac{3}{2+k} \mathbf{G} \cdot \boldsymbol{\rho}, \quad r < R, \quad (\text{A3})$$

$$T_f(\mathbf{r}) = \left[ 1 + \frac{1-k}{2+k} \left( \frac{R}{\rho} \right)^3 \right] \mathbf{G} \cdot \boldsymbol{\rho}, \quad r \geq R,$$

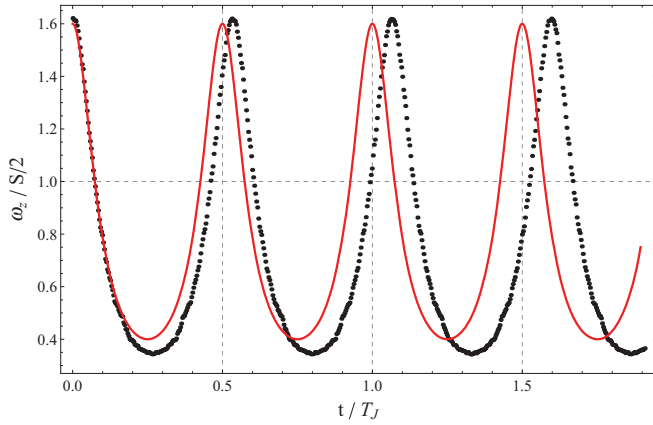


FIG. 10. (Color online) Angular velocity vs time. Solid (red) curve, theory of Jeffery [11], Eqs. (A4), for an infinite domain with a constant simple shear at infinity and the creeping ( $\text{Re} \rightarrow 0$ ) flow around the particle; dots, numerical results for small but finite  $\text{Re} = 0.05$ . Configuration:  $64^3$ ,  $\text{Pr} = 10$ ,  $k = 1$ ,  $r = 2$  ( $a = 14$ ,  $b = 7$ ),  $\text{Pe} = 0.5$ .

where  $\rho = \sqrt{x^2 + y^2 + z^2}$  is the distance from the particle’s center.

In our Couette flow simulations,  $\mathbf{G} = \hat{\mathbf{y}} \Delta / H$ , but the temperature boundary conditions are different from [16]. One should expect then deviations close to the walls, especially for large particles. The results are presented in Fig. 2.

### 2. Spheroid in a shear flow—“Jeffery” test

A spheroidal particle of aspect ratio  $r$  in a simple shear flow undergoes a spinning motion (in the  $XY$  plane). The angular velocity and the period of such a motion were predicted by Jeffery [11] for a case of a creeping flow around the particle,

i.e., when  $\text{Re} \rightarrow 0$ :

$$\omega_z = \frac{Sr/(r + 1/r)}{\cos^2(2\pi t/T_J) + r^2 \sin^2(2\pi t/T_J)}, \quad (\text{A4a})$$

$$T_J = 2\pi (r + 1/r) / S. \quad (\text{A4b})$$

For nonvanishing  $\text{Re}$ , the actual period of rotation of the particle deviates from that predicted by Jeffery. In Fig. 10, we compare the results of our LBM simulations with Eq. (A4a) for the case of  $r = 2$  and  $\text{Re} = 0.05$ . There is a 6% difference in periods due to a finite  $\text{Re}$ , but also due to the influence of the other particles present due to the periodic boundary conditions, and also the influence of the walls ( $2a/H \simeq 0.44$ ).

### APPENDIX B: APPROXIMATION OF NONINTERACTING PARTICLES

The approximation of noninteracting spheroids comes from simple geometrical considerations, and it is valid provided the particle aspect ratio  $r < \varphi^{-1/2}$ , as confirmed by the following derivation:

$$\begin{aligned} \varphi &= \frac{V_{\text{all particles}}}{V_{\text{total}}} = \frac{N V_{\text{particle}}}{V_{\text{total}}} = \frac{V_{\text{particle}}}{V_{\text{eff}}} \\ &= \frac{4\pi a b^2 / 3}{V_{\text{eff}}} = \frac{4\pi a b^2 / 3}{\mathcal{L}^3} = \frac{4\pi a^3 r^{-2} / 3}{\mathcal{L}^3} \Rightarrow \\ \mathcal{L} &= \sqrt[3]{\frac{4\pi a^3 r^{-2} / 3}{\varphi}} = a \sqrt[3]{\frac{4\pi}{3r^2 \varphi}}, \\ 2a < \mathcal{L} &\Rightarrow r < \sqrt{\frac{\pi}{3\varphi}} \Rightarrow r < \varphi^{-1/2}. \quad (\text{B1}) \end{aligned}$$

Here  $N$  is the number of particles in the total volume (of fluid and particles together),  $V_{\text{total}}$ ,  $V_{\text{eff}} = V_{\text{total}}/N$  is an “effective” volume per particle, and  $\mathcal{L} = V_{\text{eff}}^{1/3}$  is a characteristic length/dimension of the effective box/volume embedding the particle.

[1] J. Fan and L. Wang, *J. Heat Transf.* **133**, 040801 (2011).  
 [2] C. Kleinstreuer and Y. Feng, *Nanoscale Res. Lett.* **6**, 229 (2011).  
 [3] J. H. Lee, S. H. Lee, C. J. Choi, S. P. Jang, and S. U. S. Choi, *Int. J. Micro-Nano Scale Transp.* **1**, 269 (2010).  
 [4] J. Buongiorno, D. C. Venerus, N. Prabhat, T. McKrell, J. Townsend, R. Christianson, Y. V. Tolmachev, P. Koblinski, L.-w. Hu, J. L. Alvarado, I. C. Bang, S. W. Bishnoi, M. Bonetti, F. Botz, A. Cecere, Y. Chang, G. Chen, H. Chen, S. J. Chung, M. K. Chyu, S. K. Das, R. Di Paola, Y. Ding, F. Dubois, G. Dzido, J. Eapen, W. Escher, D. Funfschilling, Q. Galand, J. Gao, P. E. Gharagozloo, K. E. Goodson, J. G. Gutierrez, H. Hong, M. Horton, K. S. Hwang, C. S. Iorio, S. P. Jang, A. B. Jarzebski, Y. Jiang, L. Jin, S. Kabelac, A. Kamath, M. A. Kedzierski, L. G. Kieng, C. Kim, J.-H. Kim, S. Kim, S. H. Lee, K. C. Leong, I. Manna, B. Michel, R. Ni, H. E. Patel, J. Philip, D. Poulidakos, C. Reynaud, R. Savino, P. K. Singh, P. Song, T. Sundararajan, E. Timofeeva, T. Triticak, A. N. Turanov, S. Van Vaerenbergh, D. Wen, S. Witharana, C. Yang, W.-H. Yeh, X.-Z. Zhao, and S.-Q. Zhou, *J. Appl. Phys.* **106**, 094312 (2009).

[5] S. Özerinç, S. Kakaç, and A. G. Yazicioğlu, *Microfluidics Nanofluidics* **8**, 145 (2009).  
 [6] J. A. Eastman, U. S. Choi, S. Li, L. J. Thompson, and S. Lee, *Enhanced Thermal Conductivity Through the Development of Nanofluids*, 1996 Fall Meeting of the Materials Research Society, Boston (MRS, Pittsburgh, 1996), p. 1.  
 [7] S. Kabelac and J. F. Kuhnke, *Annals of the Assembly for International Heat Transfer Conference* (Begell House, Redding, CT, 2006), Vol. 13, p. KN.  
 [8] C.-W. Nan, R. Birringer, D. R. Clarke, and H. Gleiter, *J. Appl. Phys.* **81**, 6692 (1997).  
 [9] R. T. Bonnecaze and J. F. Brady, *Proc. R. Soc. London, Ser. A* **432**, 445 (1991).  
 [10] A. S. Sangani and A. Acrivos, *Intl. J. Multiphase Flow* **8**, 343 (1982).  
 [11] G. B. Jeffery, *Proc. R. Soc. London A* **102**, 161 (1922).  
 [12] L. G. Leal and E. J. Hinch, *J. Fluid Mech.* **46**, 685 (1971).  
 [13] E. J. Hinch and L. G. Leal, *J. Fluid Mech.* **52**, 683 (1972).  
 [14] M. P. Allen and D. J. Tildesley, *Computer Simulation of Liquids* (Oxford University Press, Oxford, 1987).

- [15] S. Succi, *The Lattice Boltzmann Equation for Fluid Dynamics and Beyond (Numerical Mathematics and Scientific Computation)* (Oxford University Press, New York, 2001), p. 304.
- [16] L. D. Landau and E. M. A. Lifshitz, *Course in Theoretical Physics—Fluid Mechanics* (Pergamon Press, London, New York, 1987).
- [17] D. J. Jeffrey, *Proc. R. Soc. London, Ser. A* **335**, 355 (1973); **338**, 503 (1974).
- [18] Y. C. Chiew and E. D. Glandt, *Chem. Eng. Sci.* **42**, 2677 (1987).
- [19] J. C. Maxwell, *Electricity and Magnetism*, 1st ed. (Oxford University Press, London, 1973), p. 365.
- [20] J. A. Eastman, S. R. Phillpot, S. U. S. Choi, and P. Keblinski, *Annu. Rev. Mater. Res.* **34**, 219 (2004).
- [21] J. M. Burgers, *K. Ned. Akad. Wet. Verhand. (Eerste Sectie)* **16**, 113 (1938).
- [22] T. J. Mcmillen and L. G. Leal, *J. Colloid Int. Sci.* **69**, 45 (1979).
- [23] T. J. McMillen, Ph.D. thesis, CalTech, Pasadena, CA, 1977. Direct calculation of the velocity field around a nanoparticle in terms of the spherical harmonics, Eq. (16), p. 108.
- [24] A. J. C. Ladd, *J. Fluid Mech.* **271**, 285 (2006).
- [25] X. He, S. Chen, and G. Doolen, *J. Comput. Phys.* **146**, 282 (1998).
- [26] [http://en.wikipedia.org/wiki/Message\\_Passing\\_Interface](http://en.wikipedia.org/wiki/Message_Passing_Interface).
- [27] Z. Guo, C. Zheng, and B. Shi, *Phys. Rev. E* **65**, 046308 (2002).
- [28] Z. Guo, B. Shi, T. S. Zhao, and C. Zheng, *Phys. Rev. E* **76**, 056704 (2007).